Full Length Article

Line-shape analysis and simulation of Er^{3+} photoluminescence spectra in erbium-stabilized nanocrystalline zirconia structures

Roberto Francini [a], Fabio De Matteis [a,*], Zoryana Zhuchenko [b], Arkadiy Zolotovsky [b], Yuriy Bacherikov [b], Georgiy Tarasov [b]

[a] *Industrial Engineering Department, University of Rome Tor Vergata, Via Del Politecnico 1, 00133, Rome, Italy*
[b] *Institute of Semiconductor Physics, National Academy of Sciences of Ukraine, Prospect Nauki 45, 03028, Kiev, Ukraine*

ABSTRACT

Peculiarities of the near-infrared and visible up-conversion spectra of nanocrystalline $(Er_2O_3)_x (ZrO_2)_{1-x}$ have been studied. It is shown that for the samples with $0.026 < x < 0.143$ the photoluminescence spectra of Er^{3+} are defined a by similar erbium environment in spite of the different symmetry of the host ZrO_2 matrix. The low temperature and room temperature emission bands in the spectral range of the $^4I_{13/2} \rightarrow {}^4I_{15/2}$ transition are measured and interpreted in terms of the multi-electron molecular orbitals cluster model developed for the case of nanocrystal structures. The role of the intra-manifold $^4I_{13/2}$ relaxation caused by the spatial confinement effects in erbium-stabilized nanocrystalline zirconia is discussed.

1. Introduction

Erbium-doped zirconia nanocrystals are recognized to be a very promising material for numerous photonic applications [1–7]. They combine the advantages of fast oxygen conductor with the rich energy level structure of trivalent erbium ions and the photoluminescence (PL) efficiency enhanced due to the small dimensions of nanostructures. Ionic conductivity is provided by mobile oxygen vacancies introduced by aliovalent dopant atoms for charge compensation [8]. These movable vacancies play a substantial role in the formation of the nearest environment of the Er^{3+} ions thus influencing the intra-atomic relaxation. Another agent favoring the relaxation process is the phonon subsystem of the host material. The phonon properties of the three low pressure (cubic, tetragonal, and especially monoclinic) phases of ZrO_2 are different and different are the related dielectric properties [9]. At the same time, it has been found that the luminescence lifetime of the $^4F_{9/2}$ excited state of Er^{3+}-ions having a concentration of 0.05 mol.% in ZrO_2 nanocrystals is very sensitive to the particle crystalline phase and size [10]. The analysis performed in Ref. [10] has shown that modifications of nonradiative relaxation mechanisms due to confinement effects are more important than the local symmetry structure of the host lattice in explaining the observed luminescence quenching. It has been shown that the confinement effects can also affect the spectroscopic properties

of rare earth ions in nanocrystals due to the cutting of the low-energy phonon modes in the 20–40 nm crystals [11]. As a result, the phonon-assisted relaxation for electrons can be restricted leaving a significant population of higher crystal field levels (contrary to Boltzmann thermal distribution) as the temperature is decreased [12]. This factor, together with many others (like pumping regime, excitation wavelength and power density, dopant concentration, temperature and radiative lifetimes of the Er^{3+} excited states) result in the complex up-conversion emissions observed in nanocrystallites [13–17] doped with Er^{3+}.

We report the near-infrared and visible up-conversion spectra of nanocrystalline $(Er_2O_3)_x (ZrO_2)_{1-x}$ prepared by the sol-gel method. Here erbium acts both as the stabilizer agent and as a supplier of Er^{3+} ions in zirconia nanocrystals. The spectra are measured at various temperatures with the purpose of detecting the phonon influence on the intra-*J*-manyfold relaxation in the Er^{3+} ions.

2. Samples and experimental details

Er_2O_3- stabilized ZrO_2 samples $(Er_2O_3)_x (ZrO_2)_{1-x}$ with composition x = 0.026, 0.053, 0.099 and 0.143 have been grown by precipitation with ammonia solution of Zirconyl chloride octahydrate (98% Aldrich) and erbium chloride hexahydrate (99.9% Aldrich). The resulting

hydrous compounds were calcined in flowing air at 1000 °C. The samples were characterized by XRD Rietveld analysis as described in Ref. [18]. The composition, structure and average crystallite sizes of the various samples are summarized in Table 1.

Samples S5, S10, and S25 were obtained through the same processing. Samples Sez10 and Sez18 belong to another batch, prepared with the same method. As one can see, sample S10 has the same Er_2O_3 content as the sample Sez10 but a different phase composition. The reason is still unclear. It is seen that the samples contain various phases: monoclinic/tetragonal, tetragonal/cubic, and purely tetragonal or cubic. Thus one can expect significant differences in the Photo-Luminescence (PL) and up-conversion PL spectra of different samples. For the spectroscopic investigations, the powder samples were manually pressed inside a plastic washer and were held in place by two fused-silica microscope slides, one of which served both as input window for the exciting laser beam and as output window for the collection of the luminescence.

All measurements were performed by exciting the erbium ions at 980 nm using an InGaAsP laser diode in continuous-wave operation. The maximum laser power was about 400 mW. The laser beam was weakly focused on the sample to a spot of approximately 1 mm^2, corresponding to a power density of about 40 W/cm^2. The PL from the sample was collected and analyzed by a 30 cm focal length monochromator and detected in the visible range by a photomultiplier tube operating in single-photon counting mode. Infrared spectra were recorded by using a cooled germanium detector.

3. High-temperature experimental results

Fig. 1 shows the PL spectra of Er^{3+} doped ZrO_2 nanocrystals measured at room temperature. The PL spectra, peaked at an energy of 6532 cm^{-1} ($\lambda = 1531$ nm) are ascribed to the $^4I_{13/2} \rightarrow {}^4I_{15/2}$ transition of Er^{3+}. The relatively broad emission structure covers the spectral region from ~6100 cm^{-1} to 7000 cm^{-1}. The structure with distinct peaks results from the Stark splitting of the $^4I_{13/2}$ and $^4I_{15/2}$ levels of Er^{3+} in crystalline compounds. In general, PL bands related to the f–f transitions in erbium-doped crystals are very narrow and their number is strictly determined by the site symmetry of the active ion. The broader PL bands are typical for erbium-doped glasses [19] and their width is ascribed to the inhomogeneous broadening caused by random variations of the crystal field. In our ceramics, such variations can be related to the oxygen vacancies randomly distributed over the volume of the nanocrystal and other defects. As a result, the crystalline symmetry (space group D_{2h}^{15}-for monoclinic phase, D_{4h}^{15}-for tetragonal phase, and O_h^5-for cubic phase) can be locally violated admitting partly or full lifting of the degeneracy of J-manifold. Thus one can expect up to 7 energy levels for the $^4I_{13/2}$ state of Er^{3+} ion and 8 levels for the $^4I_{15/2}$ state, yielding at most a total of 56 PL components for the $^4I_{13/2} \rightarrow {}^4I_{15/2}$ transition in Er^{3+} ion at room temperature. These bands form the structure of the emission spectra shown in Fig. 1. What is surprising is that the PL spectra for the different crystalline symmetries and different nanoparticle sizes display the same number of peaks in the same energy position, with the exception of sample S25, where the Er^{3+} concentration is high enough to induce concentration quenching and broadening effects. This similarity suggests a similar environment for the Er^{3+} ions in the different nanocrystal matrices. In order to verify this conclusion, the up-conversion
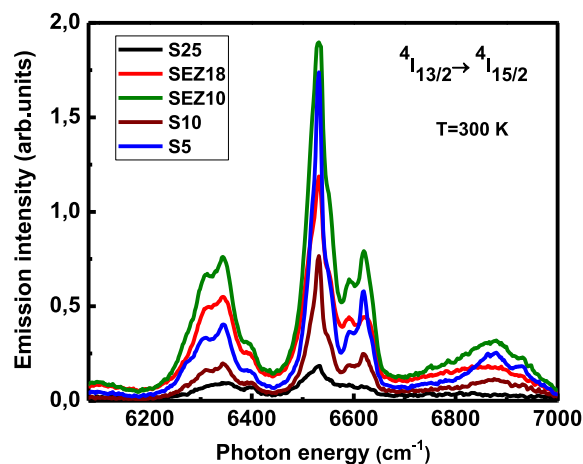

Fig. 1. Room temperature $^4I_{13/2} \rightarrow {}^4I_{15/2}$ spectra of nanocrystalline $(Er_2O_3)_x$ $(ZrO_2)_{1-x}$ for the samples from Table 1.

spectra have been measured for the same samples,

Excluding sample S25 for the above-mentioned reasons, at room temperature by pumping the $4I_{11/2}$ excited state of Er^{3+} ion at 980 nm.

In the green spectral region (Fig. 2) we observe intense emissions originating from the $^4S_{3/2}$ and $^2H_{11/2}$ excited states at 17,793 cm^{-1} and 19,032 cm^{-1} (562 nm and 525 nm), respectively. Again the similarity of
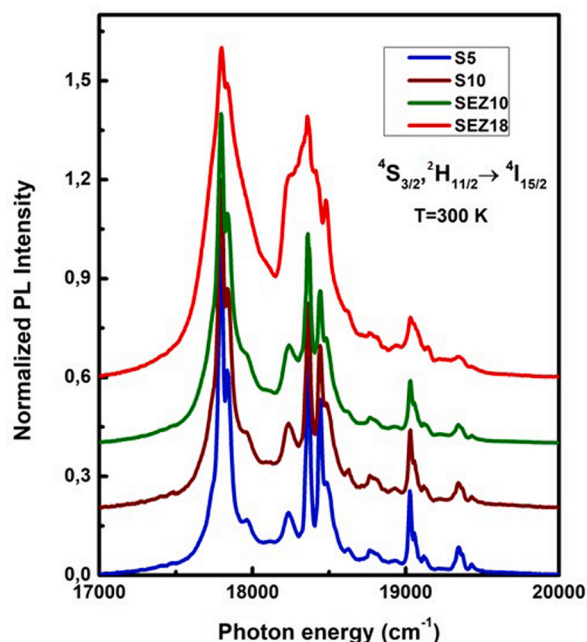

Fig. 2. Room temperature up-conversion $^4S_{3/2} \rightarrow {}^4I_{15/2}$ spectra for selected samples of different symmetry: S5 (monoclinic and tetragonal phases), S10 (tetragonal and cubic phases), SEZ10 (tetragonal phase) and SEZ18 (pure cubic phase).

Table 1
Phase composition and crystallite sizes of the investigated samples. (m = monocline t = tetragonal c = cubic).

Sample		Er_2O_3 (mol%)		Phase composition (wt%)	Er_2O_3 (mol%)	Crystallite size average) (nm)
		Nominal value	Calculated value			
S5	$Er_{0.05} Zr_{0.95} O_{1.975}$	2.6	2.9	m (12)/t (88)	0/3.4	71
S10	$Er_{0.10} Zr_{0.90} O_{1.95}$	5.3	4.8	t (80)/c (20)	4.1/7.9	77
Sez10	$Er_{0.10} Zr_{0.90} O_{1.95}$	5.3	5.7	t (100)	5.7	51
Sez18	$Er_{0.18} Zr_{0.82} O_{1.91}$	9.9	10.2	c (100)	10.2	55
S25	$Er_{0.25} Zr_{0.75} O_{1.875}$	14.3	14.5	c (100)	14.5	34

spectra for different samples is striking. The same behavior of the PL up-conversion spectra, measured with pumping the $^4I_{11/2}$ excited state of Er^{3+} ion at 980 nm, is observed at 14,720 cm^{-1} (679 nm) (Fig. 3). This strong red emission is ascribed to the $^4F_{9/2}$ excited state radiative decay to the $^4I_{15/2}$.

One can see again one-to-one correspondence between the spectral features observed both in green and red up-conversion spectra of the Er^{3+} doped ZrO_2 nanocrystals under investigation. It means that at high temperature Er^{3+} ions are subjected to the same symmetry restrictions formed by similar local environment for the crystal structures with different weights of monoclinic, tetragonal and cubic phases.

In order to describe the observed PL spectra and determine actual local symmetry of environment we apply the technique of molecular orbitals in cluster approximation developed and successfully exploited for description of rare-earth ions in various environments [20–22].

4. Cluster approximation for calculation of energy spectra of Er^{3+} in zirconium nanocrystals

The spectra of trivalent Rare-Earth Ions (REIs) in crystalline matrix have peculiar properties. Although the 4f shell, the electrons of which are responsible for optical transitions, is well screened by the electrons of completely filled 5s and 5p shells, the crystal field created by the nearest environment determines not only the fine structure of the spectrum, but also the intensities of its components. Typically, the absorption spectrum of REI embedded in a single crystal consists of a group of narrow lines. In solutions and glasses, the lines of each group are broadened and, as a rule, represent one band. The fine structure, which is the result of splitting in the crystal field of free REI levels, provides information about its local symmetry and the geometric shape of the coordination polyhedron. The nature of the fine structure of the REI spectrum in a solid has been comprehensively analyzed in Ref. [23].

The understanding of the optical properties of REIs in crystalline surrounding requires the knowledge of the REI to nearest-ligands coupling. In the pioneering work of Brecher and Riseberg [24], a simple structural model of the rare-earth environment has been proposed to describe the behavior of the first coordination shell of the Er^{3+} ion in glasses. This model predicts crystal-field parameters whose behavior well agrees with the experimentally derived values. Detailed structure arising in the absorption spectra of Er^{3+} in a phosphate matrix, associated with individual multiplet states, has been interpreted [25] using a ligand-field coordination-sphere model in order to characterize the microscopic environment surrounding the REIs in multiple sites. Similarly, analysis of REI spectra in various surrounding has been performed in other Ref. [26,27].
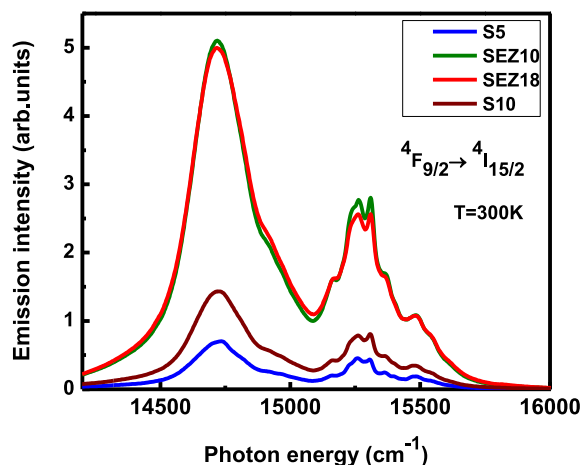

Fig. 3. Room temperature up-conversion $^4F_{9/2}{\rightarrow}4I_{15/2}$ spectra for the same samples as in Fig. 2.

To calculate the probabilities and intensities of the luminescence transitions of the REI ion in the crystal matrix, the method of multi-electron Molecular Orbitals (MO) is used. For the calculation of the energy levels of the complex, which are necessary both for the calculation of the wavelengths of optical transitions and the probabilities of transitions (as intermediate results of calculations), the MO can be constructed from the Linear Combination of Atomic Orbitals (LCAO) in the framework of the Roothaan's approach for one-electron molecular orbitals [28]. The combination of the multielectron method with an efficient and well-established one-electron method makes it possible to consistently and most simply take into account the variation of the symmetry of the ion environment, and the effect of the composition and geometry of this environment on the electronic and optical properties of the REI.

The uncompensated charge due to the bond breaking, as well as the charge of the cluster under consideration, is taken into account introducing an effective compensation potential. In this case, it is important that for the calculation of the energy levels, the Hamiltonian and local charge densities can be approximated by spherically symmetric functions. However, when calculating the probabilities of luminescence transitions, such an approximation is unacceptable, since the contributions to these probabilities come precisely from violation of spherical symmetry. Therefore for calculation of the energy levels two coordination spheres are used, and the Hamiltonian and local charge densities are approximated by spherically symmetric functions, while when calculating the probabilities of energy transitions, the first coordination sphere is taken into account, but the matrix elements of the Hamiltonian, overlap integrals, and matrix elements of electric dipole transitions are calculated without any assumptions about the spherical symmetry of the Hamiltonian and local charge densities. Thus, the quantum-chemical problem of constructing the one-electron orbitals is solved twice with different assumptions.

Multielectron atomic functions have been constructed in the nonrelativistic Hartree-Fock-Slater approximation using the Racah's technique [29]. First, the eigenfunctions and energy levels were calculated in terms of the free ion terminology. In this case, the designations of the constructed terms are conditional. We have chosen the designations corresponding to the same arrangement (numbering) of the terms of both the original and the diagonalized matrix. Moreover, there may be discrepancies in L with empirically determined terms (S and J do not differ). This is explained by the fact that the functions with different L appear in the linear combination of term functions calculated by the Hartree-Fock method, and it is impossible to assign a specific L to the "perturbed term" (due to admixture of other terms). For "perturbed" terms of higher multiplicity, the coefficient at the function of the main term is close to unity, whereas for the rest of functions these coefficients are close to zero, so that L can usually be chosen unambiguously.

Methods of theoretical analysis of atomic spectra, i.e. solutions of the many-particle problem for isolated atoms and ions are quite well documented [30,31]. By many particles in these problems, we mean unpaired electrons of partially filled shells of electrons that move in the effective central symmetric field of the nucleus and other electrons. The successes of the theory of atomic spectra are based on the theory of angular momenta and spherical tensors. Following Ref. [29] the multi-electron wave function for the f configuration can be written in the form:

$$\Psi(l^n \alpha S L M_S M_L) = \sum_{\alpha' S' L' M_{S'} M_{L'}} \Psi\left(l^{n-1} \alpha' S' L' M_{S'} M_{L'}\right) \varphi(m_s m_l)$$
$$\times \left(l^{n-1} \alpha' S' L' M_{S'} M_{L'}, l m_s m_l | l^n \alpha S L M_S M_L\right). \tag{1}$$

Hereafter s is the electron spin ($s = 1/2$), l is the orbital moment of one of the equivalent electrons (for REI $l = 3$), n is the number of equivalent electrons, S denotes the total spin of unpaired electrons, L stands for the total orbital moment of unpaired electrons, m_s, m_l, M_S, and M_L are the projections of the corresponding spin and angular moments, α is a set of

additional quantum numbers different from the angular moments (to distinguish between the ^{2S+1}L terms with the same S and L), the stroke refers to the terms (total angular momenta) of the l^{n-1} configuration over which summation is performed, finally $\varphi(m_s m_l)$ is the one-electron function of the n-th electron. Using special scheme developed in Ref. [29], the coefficients of transformation in Eq. (1) break up in a product of different factors, each of which depends only on a smaller number of variables:

$$\left(l^{n-1}\alpha' S' L' M_{S'} M_{L'}, lms_l m_l | l^n \alpha S L M_S M_L\right) = (S' s M_{S'} m_s | S' s S M_S)(L' l L M_L | L' l M_{L'} m_l)$$
$$\times \left(l^{n-1}(\alpha' S' L') l S L | \} l^n \alpha S L\right)$$
(2)

In the equation above, $(L' l M_{L'} m_l | L' l L M_L)$ and $(S' s M_{S'} m_s | S' s S M_S)$ are the Clebsch-Gordan coefficients, while $(l^{n-1}(\alpha' S' L') l S L | \} l^n \alpha S L)$ denotes the genealogical coefficients, $\Psi(l^{n-1}\alpha' S' L' M_{S'} M_{L'})$ refers to the wave function of the l^{n-1} configuration.

The multielectron atomic and then molecular orbitals have been calculated first using the technique developed in Ref. [29]. Initially, the eigenfunctions and energy levels were calculated within the framework of the terminology of free REI, using (Eq. (1)). The single-electron molecular orbitals can be constructed using one of the well-known methods of MO LCAO [28] (The method of constructing one-electron wave functions is not essential for further analysis and determines only the accuracy of the estimates). Of fundamental importance here is the construction of multi-electron functions from single-electron ones. Single-electron molecular orbital ψ_k for a complex can be presented in a form:

$$\psi_k = \sum_i \alpha_i^{(k)} f_i + \sum_{ij} \beta_{ij}^{(k)} \chi_i$$
(3)

where f_i are the f functions of the central ion, χ_i are the s and p functions of the ligands, α_i and β_{ij} are constants, k denotes a set of quantum numbers. Then we search the many-electron molecular orbitals in the form

$$\overline{\Psi}_k = \sum_{\alpha_1 \dots \alpha_n} C_{\alpha_1 \alpha_2 \dots \alpha_n}^{(k)} \psi_{\alpha_1} \psi_{\alpha_2} \dots \psi_{\alpha_n}$$
(4)

The coefficients $C_{\alpha_1 \alpha_2 \dots \alpha_n}^k$ are poly linear form from Clebsch-Gordan coefficients, genealogical coefficients and, possibly, coefficients of transition from a group of rotations to a point group of local symmetry and considered constants. To find the matrix elements of dipole transitions, using eq. (4), the matrix elements $\langle f_i | d | \chi_j \rangle$ and $\langle \chi_j | d | f_i' \rangle$ were calculated by the discrete method. In this case, the absence of spherical symmetry in the Hamiltonian is essential; otherwise, the transition probabilities would vanish. From the matrix elements in the basis of the group of local symmetry of the REI (crystalline field), we turn to the basis of spherical symmetry so the angular momentum technique can be applied. Finally, we turn to the basis of the local environment of REI. In this basis, the energy levels of REI complexes split, and the splitting is small compared to the distance between the energy levels of a free ion (for f-elements, any crystal field is weak due to screening). These split-levels are degenerate and correspond to irreducible representations of the local symmetry group of the crystal field. Matrix elements of Hamiltonian and dipole moment D can be written as

$$\langle \Psi_i' | H | \Psi_J' \rangle_{cryst} = \Gamma_{iM}^{(J)^*} \Gamma_{jM'}^{(J)} \langle JM | H | JM' \rangle_{spher}$$
(5)

and

$$\langle \Psi_i' | D_\mu | \Psi_j' \rangle_{cryst} = \Gamma_{iM}^{(J)^*} \Gamma_{jM'} Q_{\mu\nu} \langle JM | D_\nu | J'M' \rangle_{spher},$$
(6)

respectively. Here Γ is a transformation matrix from the basis of the total momentum to the basis of the crystal field. Diagonalizing the matrix $\langle \Psi_i' | H | \Psi_j' \rangle_{cryst}$, where Ψ_i and Ψ_j' are the multi-electron wave functions in

the basis of the symmetry group of the ligand field (crystal), we obtain the splitting of energy levels; D_μ is the component of the total electric dipole moment D. In this basis, the squares of the moduli of the matrix elements are the same between any two sublevels of different degenerate states. Thus, the calculated probabilities of transitions are invariant with respect to the choice of the matrix Γ.

5. Results of calculations and comparison with high temperature experimental data

Starting from the room temperature experimental PL spectra of the erbium stabilized nanocrystalline zirconia, we fit them with theoretical ones calculated for this case. It was pointed out above that the spectra for different samples are remarkably similar in spite of different crystal symmetries (see Table 1). It means that the symmetry developed in optics is different from that seen in XRD Rietveld analysis. Theoretical and experimental studies [32,33] have shown that in case of zirconia particles the relaxation of the atomic structures of nanoparticles has to be taken into account. As a result, the symmetry of relaxed $Zr_6 O_{12}$, $Zr_{10}O_{20}$, and $Zr_{14}O_{28}$ particles becomes rhombic one. We use this symmetry in our fit.

The simplest Γ matrix can be constructed for the ligand field Hamiltonian in the model of point charges, even if the point charge Hamiltonian differs from the crystal field Hamiltonian. Here only one condition must be fulfilled: the ligand field symmetry must correspond to the symmetry of the local environment of the REI. Following Ref. [34, 35] the crystal field Hamiltonian for our system can be written in a form

$$H = H_0 + V$$
(7)

Here H_0 is a Hamiltonian of free REI, and V is an electrostatic potential, which satisfies the Laplace's equation $\nabla^2 V = 0$ and has the symmetry of the environment of the ion. In this case, the potential V can be developed in a series of spherical harmonics $Y_k^q(\vartheta, \varphi)$ like [34]

$$V = \sum_{k=0}^{\infty} \sum_{q=-k}^{k} B_k^q r^k Y_k^q(\vartheta, \varphi)$$
(8)

The symmetry of the environment imposes some limitations on the coefficients B_k^q, for example, with an inversion center there are no harmonics with odd k. The simplest method of calculating this potential is the so-called point charge approximation according to which each ion is replaced by a point charge of the ion placed in the center of the ion. Further, we developed the Coulomb potential in a series over 5 spheres around the central ion. Besides B_k^q we need also to calculate the radial integrals $\langle r^k \rangle$ [34]:

$$\langle r^k \rangle = \int_0^{\infty} |f_i(r)| r^k r^2 dr$$
(9)

where $f_i(r)$ is a radial wavefunction in Hartree-Fock approximation. Results of calculation of crystal field Hamiltonian for Er^{3+} in ZrO_2 nanocrystals are presented in Tables 2 and 3.

We used these parameters to estimate the intensities of luminescence transitions in the frame of improved Judd-Ofelt method [37,38] for a

Table 2
Parameters B_k^q expressed in cm $^{-1}$ for Er^{3+} in ZrO_2 (Wybourne normalization [36]).

B_k^q	Er^{3+}
B_2^0	228
B_4^0	−687
B_4^4	758
Re B_6^4	506
Im B_6^4	19.8

Table 3
Radial integrals for Er^{3+} in ZrO_2.

|	k	
$\langle r^k(f) \rangle$	2	0.706
	4	1.217
	6	5.193
	k	
$\langle r^k(d) \rangle$	1	1.803
	3	7.306
	5	33.924
	k	
$\langle r^k(f) \rangle$	1	0.534
	3	2.868
	5	19.306

comparison with the quantum chemical method. This comparison confirms the correctness of our results.

Results of calculation of the crystal field split for the Er^{3+} ion manifolds are shown in Fig. 4 for $^4I_{13/2} \rightarrow {}^4I_{15/2}$ transitions and given separately in Table 4.

Using these splitting, the strengths of transitions between the J = 13/2 manifold and the J = 15/2 manifold sublevels have been calculated, thus permitting us to reproduce the PL spectra in the range of the $^4I_{13/2} \rightarrow {}^4I_{15/2}$ transitions. The comparison with the experimental room temperature measurements is shown in Fig. 5 for the case of Sez18 sample. The calculated transition intensities well reproduce the high-temperature experimental spectrum for the sample Sez18. Calculation have been performed in the hypothesis that all energy levels of the excited $^4I_{13/2}$ manifold are equally populated at room temperature. Thus the shape of spectrum is mainly determined by the strengths of individual transitions between sublevels of $^4I_{13/2}$ and $^4I_{15/2}$ manifold. As it follows from Table 4, we have totally 56 transitions which are shown in Fig. 5.

The picture changes drastically at low temperatures. Temperature induced transformation of the PL spectrum for $^4I_{13/2} \rightarrow {}^4I_{15/2}$ transition for the sample Sez18 are shown in Fig. 6.
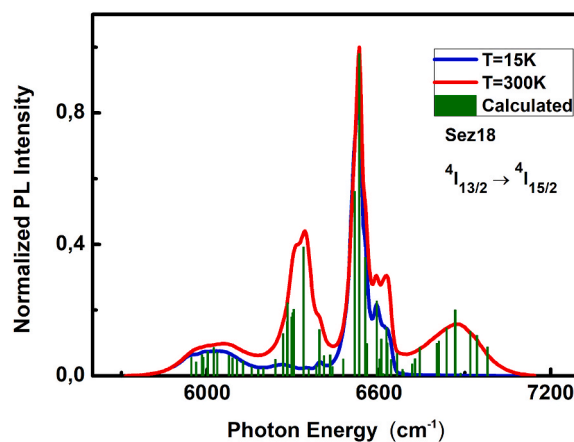
As it can be seen from Fig. 6, the high-energy wing of the PL spectrum progressively disappears and the low-energy wing transforms significantly as the temperature is decreased. The shape of the distinct PL band at 6530 cm^{-1} became more asymmetric also. The temperature-induced shift of the various PL features amount to a negligible 3 cm-1 for the whole spectral range. Such a behavior of the PL spectra under temperature changes can be describe taking into account the peculiarities of intra-manifold relaxation. Indeed, while at high temperature the excited electrons are equally distributed among the levels of the $^4I_{13/2}$ manifold, at low temperature they no-radiatively relax from higher levels to the low-lying energy levels of the same manifold. As a result, the high energy transitions disappears in the low-temperature spectrum, as shown in Figs. 5 and 6 above 6630 cm-1. Generally speaking, at temperatures
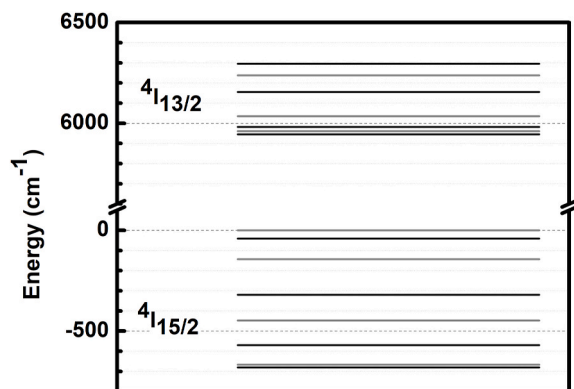
**Fig. 4.** Graphical representation of the crystal field splitting of $^4I_{13/2}$ and $^4I_{15/2}$ manifolds for ZrO_2:Er^{3+} nanocrystals with rhombic symmetry.

Table 4
Crystal-field splitting (cm^{-1}) of ^4I-manifolds for ZrO_2:Er^{3+} nanocrystals with rhombic symmetry.

^4I manifold	Crystal-Field Splitting (cm^{-1})
$^4I_{13/2}$	6295
	6238
	6155
	6035
	5982
	5961
	5945
$^4I_{15/2}$	0
	−41
	−143
	−320
	−447
	−570
	−667
	−681

Fig. 5. Normalized $^4I_{13/2} \rightarrow {}^4I_{15/2}$ spectra for the sample Sez18 at 15 K and room temperature. Normalized room temperature calculated intensities for the $^4I_{13/2} \rightarrow {}^4I_{15/2}$ transitions are shown with vertical bars.
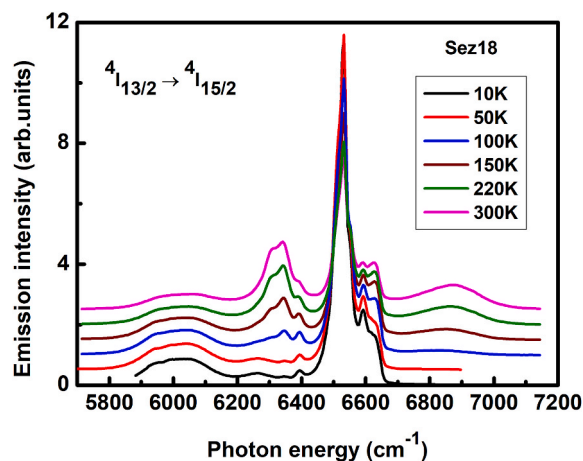
Fig. 6. The $^4I_{13/2} \rightarrow {}^4I_{15/2}$ emission spectra at different temperature for the sample Sez18.

lower than 10 K, only eight transitions should appear: from the lowest level of the excited $^4I_{13/2}$ manifold to eight levels of split $^4I_{15/2}$ manifold.

In order to verify this suggestion let us consider the low-temperature $^4S_{3/2} \rightarrow {}^4I_{15/2}$ transitions shown in Fig. 7. The $^4S_{3/2}$ manifold normally splits by crystal field into two components, 18189.86 cm-1 and
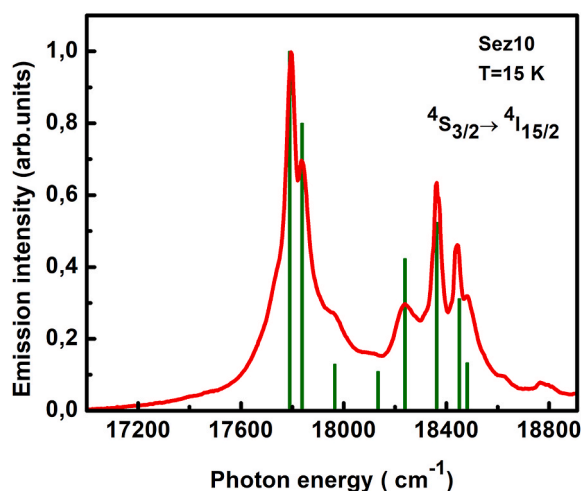
Fig. 7. Normalized low temperature up-conversion PL spectrum in the region of $^4S_{3/2} \to {}^4I_{15/2}$ transitions. Normalized calculated intensities for the same transitions are shown with vertical bars.

18490.27 cm-1, separated by 300 cm^{-1} energy gap. Therefore, in low temperature range, the transitions from low-lying energy level will dominate. For transitions from $^4S_{3/2}$ to $^4I_{15/2}$ manifold one can expect eight lines in PL spectrum. Indeed, we see corresponding spectral features at the positions of calculated transitions as shown in Fig. 7. It should be noted that the PL bands are significantly broadened due to inhomogeneity. If one substracts the energy difference between unsplit $^4S_{3/2}$ and $^4I_{13/2}$ manifolds, the low temperature PL spectra of the $^4S_{3/2} \to {}^4I_{15/2}$ and the $^4I_{13/2} \to {}^4I_{15/2}$ transitions should have similar features. We show the results of such comparison in Fig. 8, where one can see that both spectra have fairly similar features.

One can see that eight PL bands in the $^4S_{3/2} \to {}^4I_{15/2}$ spectrum are easily identified in the $^4I_{13/2} \to {}^4I_{15/2}$ spectrum as well. These bands correspond to the transitions from lowest state of $^4S_{3/2}$ and $^4I_{13/2}$ manifolds to all Stark states of $^4I_{15/2}$ manifold. It is also seen that the PL bands at 6000 cm^{-1} and at 6530 cm^{-1} in the $^4I_{13/2} \to {}^4I_{15/2}$ spectrum are complex. The PL band at 6530 cm^{-1} is significantly asymmetric as compared with that seen in $^4S_{3/2} \to {}^4I_{15/2}$ spectrum. This asymmetry is due to the additional transitions, which survived in the low-temperature regime and are related with the higher energy Stark components of $^4I_{13/2}$ manifold. Such additional energy levels are absent for the $^4S_{3/2}$ manifold
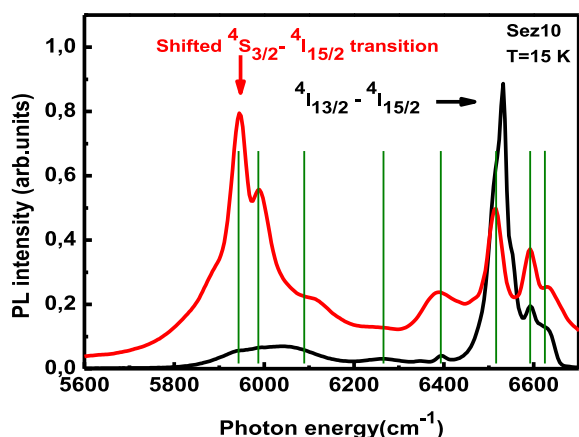
and the corresponding PL line in the $^4S_{3/2} \to {}^4I_{15/2}$ spectrum is symmetric and inhomogeneously broadened (see Fig. 8). The contribution of higher energy components of $^4I_{13/2}$ manifold can also explain a noticeable blue shift of broad PL band at 6000 cm^{-1} in the $^4I_{13/2} \to {}^4I_{15/2}$ spectrum under lowering temperature. The question is now why the low-lying energy states of $^4I_{13/2}$ manifold are still highly populated at low temperature. Let us consider the structure of the Stark splitting for $^4I_{13/2}$ manifold. As follows from Table 4 lowest energy levels are grouped in a bunch with further energy gap above it. The first four levels are separated by 16, 21 and 53 cm-1. Next level is about 120 cm-1 higher creating a specific energy gap. For effective intra-manifold relaxation, it is important the presence in the nanocrystals of phonons with suitable energy.

As it has been shown in Ref. [11] the spatial confinement in ZrO$_2$ nanocrystals leads to modification of the vibrational spectra, with the introduction of a low-energy phonon band gap in the phonon dispersion branches. The appearance of such gap hinders the efficient phonon-assisted intra-manifold relaxation responsible for the rapid thermalization of the electron level occupancy of the lowest Stark component of the J-manifolds. Thus for a certain level a phonon-bottleneck arises leading to an increase, compared to a thermal equilibrium Boltzmann distribution, of the same level population [12]. As result, the intensity of the PL band related to this particular level significantly enhances under temperature lowering, and this fact explains the 6530 cm-1 PL feature of the low temperature $^4I_{13/2} \to {}^4I_{15/2}$ transition. Therefore, we ascribe the asymmetry of this feature to low-temperature hot PL bands. Temperature elevation increases the phonon density with an increase of the inelastic scattering. This scattering bridges the energy gap for the electron relaxation as the temperature is increased, yielding the rapid depopulation of the higher levels. We therefore assume that the dominant mechanism of carrier population deviation from thermal equilibrium in $(Er_2O_3)_x$ $(ZrO_2)_{1-x}$ nanocrystals is the phonon restriction, caused by the lack of low-energy phonons needed for effective carrier transfer between closely lying energy levels of the $^4I_{13/2}$ manifold.

6. Conclusions

Different sol-gel grown $(Er_2O_3)_x$ $(ZrO_2)_{1-x}$ nanostructures stabilized with Er^{3+} ions have been optically investigated by means of photoluminescence and up-conversion techniques. The investigation of high-temperature near-infrared and visible up-conversion spectra has shown that for the samples with $0.026 < x < 0.099$ the photoluminescence spectra of Er^{3+} are defined by similar erbium environment in spite of different symmetry of the host ZrO$_2$ matrix. The low-temperature spectra ascribed to the $^4I_{13/2} \to {}^4I_{15/2}$ transitions in Er^{3+} reveal some peculiarities which cannot be understand without knowledge of the crystal-field splitting of $^4I_{13/2}$ and $^4I_{15/2}$ manifolds. These manifolds are especially important since they are the working levels for Er-based lasers. Therefore, the simulations of the spectra involving transitions among these manifolds have been carried out. The simulation has been performed using multi-electron molecular orbitals cluster model developed for the case of nanocrystal structures. Both energy levels and probabilities of transitions among the split levels have been calculated in order to successfully reproduce the PL lineshape for the $^4I_{13/2} \to {}^4I_{15/2}$ transitions. We demonstrate the existence of a peculiar energy gap in the level distribution of the $^4I_{13/2}$ manifold. Taking into account possible absence of low-energy phonons in the phonon spectrum of spatially confined structures, the energy restricted relaxation (so called phonon bottleneck) is expected for $^4I_{13/2}$ manifold. This mechanism is the origin of the observed "hot PL bands" in the low-temperature PL spectra in the range of the $^4I_{13/2} \to {}^4I_{15/2}$ erbium transitions.

Credit author contribution statement

Roberto Francini: Investigation, Writing-review&editing,

Fig. 8. The low-temperature PL spectra of $^4S_{3/2} \to {}^4I_{15/2}$ and $^4I_{13/2} \to {}^4I_{15/2}$ transitions. The spectrum $^4S_{3/2} \to {}^4I_{15/2}$ is obtained from that shown in Fig. 7 by subtracting the energy distance between $^4S_{3/2}$ and $^4I_{15/2}$ manifolds. Vertical lines stand for the calculated energies of transitions from the lowest state of $^4S_{3/2}$ and $^4I_{13/2}$ manifold to all Stark states of $^4I_{15/2}$ manifold.

References

[1] G. Chen, G. Somesfalean, Y. Liu, Z. Zhang, Q. Sun, F. Wang, Upconversion mechanism for two-color emission in rare-earth-ion-doped nanocrystals, Phys. Rev. B 75 (2007), 195204.

[2] A. Patra, C.S. Friend, R. Kapoor, P.N. Prasad, Upconversion in Er^{3+}:ZrO$_2$ nanocrystals, J. Phys. Chem. B 106 (2002) 1909–1912.

[3] E. De la Rosa-Cruz, L.A. Díaz-Torres, R.A. Rodríguez-Rojas, M.A. Meneses-Nava, O. Barbosa-García, Luminescence and visible upconversion in nanocrystalline ZrO2:Er3+, Appl. Phys. Lett. 83 (2003) 4903.

[4] P. Salas, C. Angeles-Chávez, J.A. Montoya, E. De la Rosa, L.A. Diaz-Torres, H. Desirena, A. Martínez, M.A. Romero-Romo, J. Morales, Synthesis, characterization and luminescence properties of ZrO2: Yb3+–Er3+ nanophosphor, Opt. Materials 27 (2005) 1295–1300.

[5] A. Patra, C.S. Friend, R. Kapoor, P.N. Prasad, Effect of crystal nature on upconversion luminescence in Er3+:ZrO2 nanocrystals, Appl. Phys. Lett. 83 (2003) 284–286.

[6] L.A. Díaz-Torres, E. de la Rosa-Cruz, P. Salas, C. Angeles-Chavez, Concentration enhanced red upconversion in nanocrystalline ZrO$_2$: Er under IR excitation, J. Phys. D: Appl. Phys. 37 (2004) 2489–2495.

[7] E.K. Barimah, S. Rahayu, M.W. Ziarko, N. Bamiedakis, I.H. White, R.V. Penty, G. M. Kale, G. Jose, Erbium-doped nanoparticle–polymer composite thin films for photonic applications, Structural and Optical Properties" A*CS Omega* 5 (16) (2020) 9224–9232, 2020.

[8] F. Pietrucci, M. Bernasconi, C. Di Valentin, F. Mauri, C.J. Pickard, EPR g-tensor of paramagnetic centers in yttria-stabilized zirconia from first-principles calculations, Phys. Rev. B 73 (2006), 134112.

[9] X. Zhao, D. Vanderbilt", Phonons and lattice dielectric properties of zirconia", Phys. Rev. B 65 (2002), 075105.

[10] G.S. Maciel, A. Patra, Influence of nanoenvironment on luminescence lifetime of Er^{3+}-activated ZrO$_2$ nanocrystals, J. Opt. Soc. Am. B 21 (2004) 681–684.

[11] G.K. Liu, H.Z. Zhuang, X.Y. Chen, Restricted phonon relaxation and anomalous thermalization of rare earth ions in nanocrystals, Nano Lett 2 (2002) 535–539.

[12] J.J.H.A. van Hest, G.A. Blab, H.C. Gerritsen, C. Mello Donega, Andries Meijerink, The role of a phonon bottleneck in relaxation processes for ln-doped NaYF$_4$ nanocrystals, J. Phys. Chem. C 122 (7) (2018) 3985–3993.

[13] Z. Yang, J. Luo, S. Yang, Q. Wu, Fabrication of ZrO2:Er3+ nanocrystals and the researching of emitting mechanism, Energy Proc. 17 (2012) 305–310.

[14] K. Smits, D. Olsteins, A. Zolotarjovs, K. Laganovska, D. Millers, R. Ignatans, J. Grabis, Doped Zirconia Phase and Luminescence Dependence on the Nature of Charge Compensation" Scientific Reports7, 2017, 44453.

[15] F. Vetrone, J.C. Boyer, J.A. Capobianco, A. Speghini, M. Bettinelli, NIR to visible upconversion in nanocrystalline and bulk Lu2O3: Er3+, J Phys Chem B 106 (22) (2002) 5622–5628.

[16] J.A. Capobianco, F. Vetrone, J.C. Boyer, A. Speghini, M. Bettinelli, Enhancement of red emission (4F9/2→ 4I15/2) via upconversion in bulk and nanocrystalline cubic Y2O3: Er3+", J. Phys. Chem. B 106 (2002) 1181–1187.

[17] R. Francini, S. Pietrantoni, M. Zambelli, A. Speghini, M. Bettinelli, Upconversion dynamics in Er3+ doped nanocrystalline YAlO3, J. Alloys Compd. **380** (2004) 34–38.

[18] P. Riello, S. Bucella, R. Krsmanovic, S. Meneghetti, S. Pietrantoni, R. Francini "Synthesis, X-ray diffraction characterization, and radiative properties of Er2O3 – ZrO2 nanocrystals embedded in LAS glass ceramics, J. Phys. Chem. B 109 (2005), 13424.

[19] R. Francini, U.M. Grassano, G.G. Tarasov, Broadening of Er3+ electronic states in phosphate glasses, J. Chem. Phys. 115 (2001) 7975.

[20] A.A. Zolotovsky, Energy Spectrum of Rare-Earth Ions (Tm3 +, Tb3 +, Sm3 +) in Sulfide and Oxide Matrices in the Cluster Approximation, PhD thesis, Kiev, 2007.

[21] S. Pinelli, R. Francini, A.A. Zolotovsky, G.G. Tarasov, A. Speghini, M. Bettinelli, Line-shape analysis of optical spectra in metaphosphate glasses doped with erbium ions, Chem. Phys. 321 (2006) 91–99.

[22] N. Korsunska, L. Borkovska, L. Khomenkova, T. Sabov, O. Oberemok, O. Dubikovsky, Z. Ya Zhuchenko, A. Zolotovsky, I.N. Demchenko, Y. Syryanyy, C. Guillaume, C. Labbe, X. Portier, Redistribution of Tb and Eu ions in ZnO films grown on different substrates under thermal annealing and its impact on Tb-Eu energy transfer, Appl. Surf. Sci. 528 (2020), 146913, 30 October.

[23] C. Görller-Walrand, K. Binnemans, Rationalization of crystal-field parametrization, in: K.A. Gscheidner Jr., L. Eyring (Eds.), Handbook on the Physics and Chemistry of Rare Earths, North-Holland, Amsterdam, 1996, pp. 121–283. .2, ch. 155.

[24] C. Brecher, L.A. Riseberg, Laser-induced fluorescence line narrowing in Eu glass: a spectroscopic analysis of coordination structure, Phys. Rev. B 13 (1976) 81.

[25] J.B. Gruber, D.K. Sardar, B. Zandi, J.A. Hutchinson, C.W. Trussell, Modeling the absorption spectra of Er3+ and Yb3+ in phosphate glass, J. Appl. Phys. 8 (2003) 4835–4840.

[26] K. Ueda, S. Tanaka, T. Yoshino, Y. Shimizu, T. Honma, Site-selective doping and site-sensitive photoluminescence of Eu3+ and Tb3+ in perovskite-type LaLuO3, Inorg. Chem. 58 (16) (2019) 10890–11089.

[27] M. Behrendt, S. Mahlik, K. Szczodrowski, B. Kukliński, M. Grinberg, Spectroscopic properties and location of the Tb3+ and Eu3+ energy levels in Y2O2S under high hydrostatic pressure, Phys. Chem. Chem. Phys. 18 (2016) 22266–22275.

[28] C.C.J. Roothaan, New developments in molecular orbital theory, Rev. Mod. Phys. 23 (2) (1951) 69–89.

[29] G. Racah, Theory of complex spectra III, Phys. Rev. V. 63 (№ 1) (1943) 367–382. G. Racah, Theory of complex spectra IV, Phys. Rev. V.76, № 8, pp.1352–1365 (1949).

[30] S. Lehtola, A review on non-relativistic, fully numerical electronic structure calculations on atoms and diatomic molecules, Int. J. Quant. Chem. 119 (Is.19) (2019), e25968.

[31] M.C. Zerner, Perspective on "New developments in molecular orbital theory. Roothaan CCJ, Rev. Mod. Phys. 23 (1951) 69–89. Theor. Chem. Acc. 103, 217-218 (2000).

[32] S. Tsunekawa, S. Ito, Y. Kawazoe, J.-T. Wang, Critical size of the phase transition from cubic to tetragonal in pure zirconia nanoparticles, Nano Lett. 3 (7) (2003) 871.

[33] V.G. Zavodinsky, A.N. Chibisov, Zirconia nanoparticles and nanostructured systems, J. Phys.: Conf. Ser. 29 (2006) 33.

[34] A. Abragam, B. Bleaney, Electron paramagnetic resonance of transition ions, Oxford Classic Texts in the Phys Sci. 2 (2012) 317.

[35] P. Novak, K. Knížek, J. Kuneš, Crystal field parameters with Wannier functions: application to rare-earth aluminates, Phys. Rev. B 87 (2013) 205139, 7.

[36] B.G. Wybourne, Spectroscopic Properties of Rare Earth, Interscience, New York, 1965.

[37] B.R. Judd, Optical absorption intensities of rare earth ions, Phys. Rev. 127 (1962) 750–761.

[38] G.S. Ofelt, Intensities of crystal spectra of rare-earth ions, J. Chem. Phys. 37 (1962) 511–520.